Ultraspectral: Hyperspectral and RF Features Registered by IFSAR

Harold Szu[*a], *Charles Hsu*[**b]
[a]*Digital Media RF Lab, The George Washington University, Washington DC 20052*
[b]*Trident Systems Inc., Fairfax, Virginia 22030*

ABSTRACT

Hyperspectral remote sensing by air platforms can passively generate over two hundred channels of images of terabyte data the ground surface reflectance/eminence simultaneously, with wavelength ranging from 0.4 to 2.5 μm and to include a full infrared spectrum. We have extended the hyperspectral to include RF spectral for both the foliage penetration (from L band 1 GHz to UHF band 0.5 GHz,) using the polarization RF features and the terrain location ID for automatic navigation registration. These generalizations are possible because we have based our design of the foliage penetration (FOPEN) Interferometric Synthetic Aperture Radar (IFSAR) on all digital transceiver array and Field Programmable Gate Arrays (FPGA). We are able to do that, since we have leveraged the ONR 100 dB Digital Array Radar (DAR) for shipboard volume search radar (VSR) using the matured & rugged GaAs cellular phone technology [1]. We study whether the high dynamic range DAR VSR approach can overcome the long baseline terran curvature (that might otherwise not be suited for the FOLPEN low frequency IFSAR). We show the standard deviation of the phase digital resolution better then 1^o might overcome the terrain curvature due to low frequency, and long time integration. The applications of this technology include environmental monitoring and mineral exploration and mining, communication and Aided Target Recognition (ATR). The hyperspectral imagery takes the advantage of more unique spectral signature in terms of the massively parallel artificial neural network computation using the unsupervised learning Independent Component Analyses (ICA) algorithm introduced to the Landsat by Szu [2, 3] The supervised classification is based on the library of spectral signals of known object material characteristics using various constrained versions of the orthogonal subspace projections (OSP) by [7, 8]. In this paper, we combine both the supervised OSP and the unsupervised ICA hyperspectral imaging algorithms. Then, we present all digital version of FOPEN SAR, considered as one of RF channels in ultraspectral image processing. Taking the advantage of the high dynamic range ONR DAR VSR technology, we can measure both RF signatures and 3D terrain by means of Interferometric (IF) FOPEN SAR. We prefer a real-time one-path fly over using bi-static Interferometric SAR equipped with a Stokes polarization vector information that can provide us with not only the RF signatures but also terrain height for location ID (knowing terran contour map stored in the flight data basis). Such an ultraspectral imaging feature-fusion system can manage Forrest search and rescue when it is complement IFSAR FOPEN with high-resolution EO/IR signatures. Conclusion and discussion are given in the final section.

1. INTRODUCTION

As the amount of data associated with hyperspectral remotely sensing is growing exponentially, earth scientists require more efficient ways to search and analyze such data. In particular, extracting image content by both EO/IR and RF features is emerging as one of the most demanded tools to perform data mining. One of the most promising methods to extract image content is via ultraspectral feature classification, which provides a set of ranking labeling of each pixel in the image. Figure 1 briefs the early DARPA notion of Hyperspectral. From Figure 1, it reveals the need of FOPEN & IF-SAR for mountain terrain masked by the forest.

The traditional classification scheme that is based on the winner-take-all strategy of which only one majority class label is selected within each pixel may not be adequate in some resource management application. Wherever there is uncertainty due to more equally probable classes, we can obviously take the advantage of neighborhood spectral consistency into consideration by enlarging the single pixel voting committee multi spectral bands to including four nearest neighborhood spectral bands and thus gain a few percentage to improve the result, as shown by Szu & Telfer [4,5]. On the other hand, a systematical check of all neighborhood spectral consistency can be done with the help of a local texture Fourier-like transform without a window, namely the so-called wavelet transform by Szu, et al. [3]. In our recent effort, we have addressed the necessity of unsupervised learning neural network technology for the surveillance of tropical rain forest deforestation, for which we need to know at the forest boundary pixel the unknown percentage of tree content of each pixel of a foot print of 30x30 squared meters, i.e. multiple labels with variable percentages [2, 3]. In the remote sensing, the light

Wavelet Applications VIII, Harold H. Szu, David L. Donoho, Adolf W. Lohmann, William J. Campbell,
James R. Buss, Editors, Proceedings of SPIE Vol. 4391 (2001) © 2001 SPIE. · 0277-786X/01/$15.00

reflected from the sun and the thermal energy emitted from the earth have broad spectra measured at the focal plan on a high altitude space satellite that help classify the large scale canopy on the ground. While the weather satellite, AVHRR of NOAA, has five spectral bands, the Landsat of NASA has seven spectral bands, ranging from the green light at 0.5μm wavelength to mid infrared 3 to 5μm to the long infrared light about 10 to 12μm wavelength. Since the remote sensing is continuous on board of a geo-synchronous satellite rotation with the earth at a high altitude, each picture element (pixel) covers a large area on the earth by the Landsat (or 1.1 kilometers by the weather satellite AVHRR) of which multiple labels are desirable of each pixel.

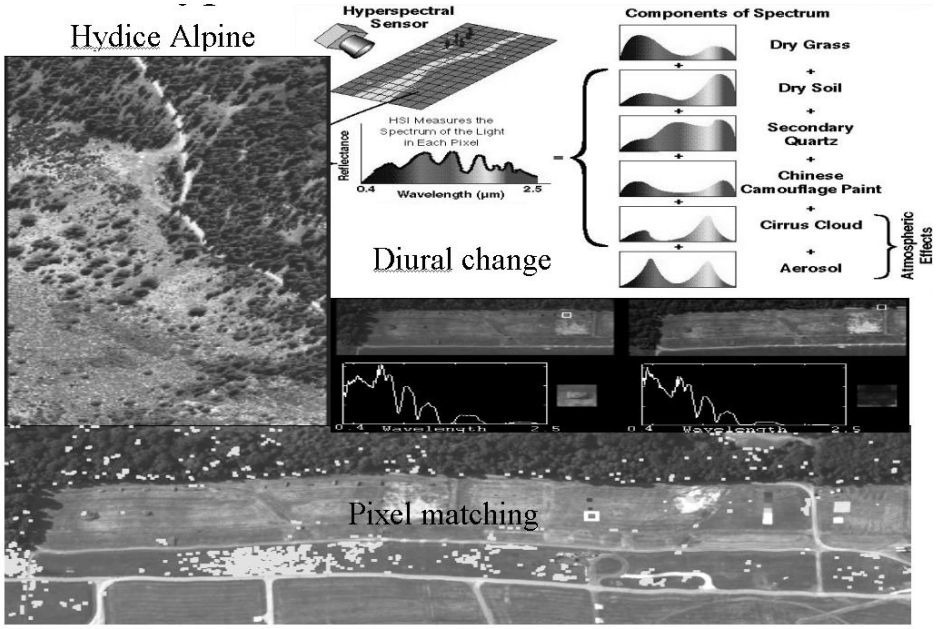

Figure 1. Hyperspectral data of EO/IR, it reveals the need of FOPEN & IFSAR for mountain terrain masked by the forest.

Hyperspectral image sensors provide spectral images with several hundred channels per pixel that enable the information extraction about different materials within a pixel. Previous approaches e.g. spectral mixture modeling of Adams and Smith [9, 10] demix spectrally different materials at a sub-pixel level by assuming that basic spectral knowledge of the main material of interest (called endmembers) is known and that the spectrum is mainly composed of these materials. These assumptions may not be true due to incomplete knowledge of spectral scene, leading to incorrect results [9, 11]. A more recent approach by Maselli, Pieri, and Conese [12] avoids this problem by using specially chosen pixels from the scene as endmembers. After a cluster analysis of the scene, maximum likelihood classification is used to pick up the pixels, which are most representative of the typical spectral features of the clusters and therefore pixels are chosen as endmembers. Unfortunately, the pixels chosen as endmembers may consist of mixtures themselves. Thus, it remains very difficult to determine the real endmembers in a scene without prior knowledge of the scene. Recently, Orthogonal Subspace Projection (OSP) [7, 8] approach was developed, which have shown some success in hyperspectral image classification and subpixel detection. OSP separates the undesired targets from the desired targets, and then uses an orthogonal subspace projector to eliminate the undesired targets prior to classifying the desired targets. An assumption made in the OSP approach is that the knowledge of both the desired and undesired target signatures must be known *a priori*. Such information is generally difficult to obtain in practice.

In order to address this issue, we note that the determination of endmembers may be viewed as a specific case of the blind source separation (BSS) problem. In this paradigm, the data consists of linearly mixed signals and the goal is to determine which minerals are being mixed without prior knowledge of what minerals are in a scene. A relatively new unsupervised neural network, ICA introduced by Szu [2,3,5,6], approximates the solution to this problem by assuming independence of the spectral information for different materials in the limit of large number of spectral channels. This strong assumption gives ICA the ability to use all of the statistics in the mixed signal rather than just first order (the mean), second order (the covariance), or fourth order (Kurtosis) statistics.

Image feature fusion is a way of combining the spectral information of a coarse-resolution image with the spatial resolution of a finer image. The result is a product that synergistically combines the best features of each of its components. Good combinations of fused imagery include Landsat 7 ETM+ multispectral/panchromatic, Landsat TM/SPOT panchromatic, Landsat TM/IRS 1-C panchromatic and SPOT multispectral/SPOT panchromatic. The color hue of Landsat determines the SPOT sat geometry.

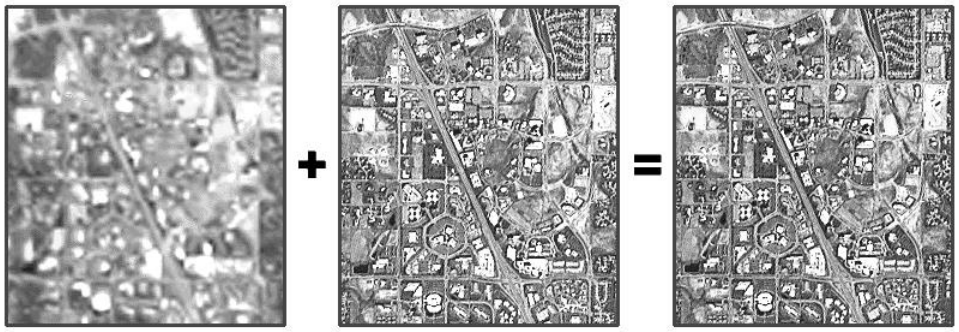

Figure 2. An example of image feature fusion using 7-Spectral ID and 3-spectral SPOT Geometry (Source: *I-cubed Information, Integration & Imaging, Fort Collins, CO 80524*)

The paper will be organized as follows. Introduction is presented in the first section. Then, the hyperspectral imaging technologies are reviewed. Some comparisons are included in the second section as well. Next, the hardware implementation of FOPEN SAR is presented. IFSAR is discussed conceptually and we analyze the phase difference of the focused images to provide an interferometric system for the higher elevation accuracy. Finally, we conclude with the related processing: image registration, and Geocoding, which lead to the DEM in universal cartographic reference systems.

2. HYPERSPECTRAL IMAGING PROCESSING

Target detection and classification in an unknown environment is generally difficult. This is particularly true for hyperspectral surveillance airview imagery. Since hyperspectral sensors use as many as 200 contiguous bands to uncover diagnostic narrow-band spectral features of materials with very similar spectral signatures, it is expected that a good number of substances can be exploited for discrimination and quantification. In this case, finding desired target signatures present in an image could be very challenging. An early attempt was made to use vector quantization to group potential objects into different clusters. This approach requires know the number of classes to be clustered [14]. A similar problem also arises in sensor array processing where An Information Theoretic Criterion (AIC) [15, 16] or Minimum Description Length (MDL) [21, 22] is generally used to determine the number of signals, but not signals themselves. These criteria may not be appropriate in determining the number of spectral components resident in multispectral or hyperspectral images. First the noise in remotely sensed imagery may not be stationary and may not even be independent identically distributed. Second, the data statistics may not be available or difficult to obtain, particularly for the likelihood functions used in these criteria.

A multispectral/hyperspectral image pixel is generally mixed by different material substances resident in the pixel and spectral de-mixing is a method that estimates the percentage of each material within the pixel. One widely used approach to subpixel detection and mixed pixel classification is linear spectral unmixing [9, 10, 18, 19]. It describes a mixed pixel as a linear mixture of all materials resident in the pixel and the spectrum of the mixed pixel vector is a linear combination of material signatures so that individual material in the pixel can be quantified and discriminated by inverting the material signature matrix. Orthogonal Subspace Projection (OSP) was developed in [20] and shown some success in hyperspectral image classification and subpixel detection. The OSP approach is primarily developed for hyperspectral image classification. It separates the undesired targets from the desired targets, and then uses an orthogonal subspace projector to eliminate the undesired targets prior to classifying the desired targets. A supervised assumption made in the OSP approach is that the knowledge of both the desired and undesired target signatures must be known *a priori*. Such information is generally difficult to obtain in practice.

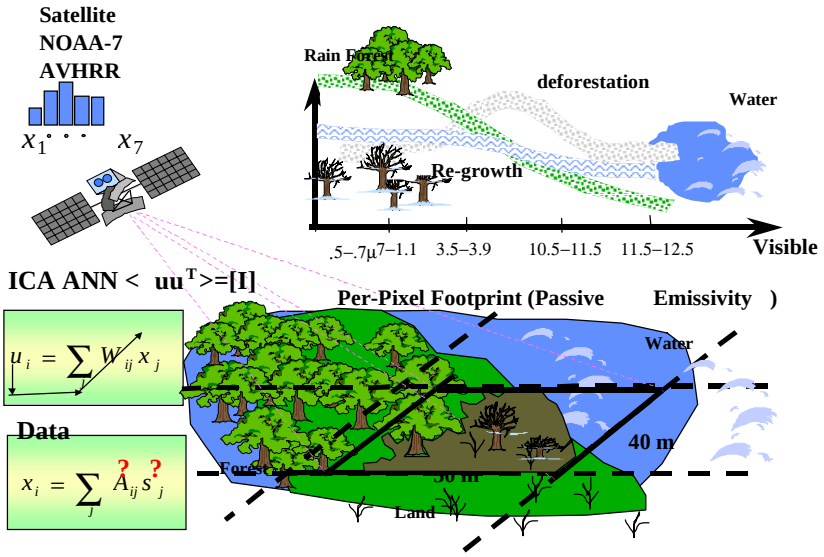

Figure 3 : Landsat remote sensing application. Reflectance matrix [A] changes daily, seasonally, and thus unkown in principle. Percentage s_j varies from pixel to pixel.

Recently Szu has applied the early vision feature extraction neural network with a truly unsupervised learning algorithm (without specification of either the number of classes and percentage value of each desired labels) to estimate the percentage of multiple-labels-per-pixel [2,3,5,6]. In [2,3,5,6], Szu extended the percentage composition study to all pixels in each region. This overcomes another source of errors due to the mismatch between the desired category and the supporting spectral signature, in the so-called "spectral-weak" category in case of grape vine in the winter season. Nevertheless, the field has a relative strong spatial lattice texture as spatial signature if we sample it with wavelets over many pixels or if we use the vision neural net to find the percentage of multiple categories within each pixel. Then, we need both macroscopically the spatial texture wavelet analyses and microscopically the sub-pixel percentage analyses. There is another Landsat remote sensing application (shown in Figure 3) demonstrated by Szu et al. at SPIE Proceedings 3723 addressing the micro-remote sensing surveillance of deforestation in ICA mapping spectral ID to statistics ID in Figure 3.

2.1 Independent Component Analysis (ICA)

As introduced by Bell, Sejnowski, Amari, Oja, and Comon [20-24], ICA approximates the factor analysis of multiple linearly mixed source signals through assuming that the sources are statistically independent from one another. This relationship can be explained as follows. When a newborn child faces the bustling and hustling world, the child may have difficulty to recognize the changing and independent signal $\mathbf{s}_i(t) \equiv s_i(t)\mathbf{a}_i$, i=1,2,from the sensory inputs $x_1(t)$, $x_2(t)$. However, the child soon recognizes the noises (that are invariant and universal by the central limiting theorem) that have zero cross correlation $<v_1(t)v_2(t)>_G = 0$ etc. of neuron outputs and then what have been sieved within the synaptic weight matrix [W] are related to the signals. This is the intuition of being not-noise must be signals, so-called the negation of the converse logic.

Given the 7-component data vector $(x_1(t),\ldots x_7(t))^T \equiv \boldsymbol{X}(t)$ one assumes a linear and instantaneous model of signals,

$$\boldsymbol{X}(t) = s_1(t)\,\boldsymbol{a}_1 + \ldots + s_7(t)\,\boldsymbol{a}_1 \equiv [\boldsymbol{A}]\,\boldsymbol{S}(t) \qquad (1)$$

(by matrix multiplication definition) where both the source intensity $(s_1(t), \ldots, s_7(t))^T \equiv$ vector $\boldsymbol{S}(t)$ and the mixing vector directions $[\boldsymbol{a}_1, \ldots, \boldsymbol{a}_7] \equiv$ matrix $[\boldsymbol{A}]$ are unknowns**.** In other words, they may be less then seven. Thus, the artificial neural networks (ANN) seeks a linearly weighted output vector: $\boldsymbol{V}(t) \approx [\boldsymbol{W}]\boldsymbol{X}(t)$ that acts like linear whitening filters outputting nothing but the purely Gaussian noise:

$$<\boldsymbol{V}(t)\,\boldsymbol{V}(t)^T>_G = [I] \approx [\boldsymbol{W}][\boldsymbol{A}]<\boldsymbol{S}(t)\,\boldsymbol{S}^T(t)>\,[\boldsymbol{A}]^T[\boldsymbol{W}]^T \qquad (2)$$

which implies $[\mathbf{W}][\mathbf{A}] \approx [I]$ because $<\mathbf{S}(t)\,\mathbf{S}^T(t)> \approx [I]$ (3)

The concept of independence happens to behave like the noise only at the second moment, but has a nontrivial higher order statistics (HOS) (see examples later). Thus, from Eq(3), the internal knowledge representation *[**W**]* is discovered as the inverse of the external world matrix $[\mathbf{A}]^{-1}$. Mathematically speaking, this is called the Independent Component Analyses (ICA) among multiple inputs and multiple outputs. Such an edge map that is orthogonal to one another has been reproduced by a truly unsupervised learning paradigm of artificial neural networks (ANN) by maximizing the output entropy of among 10^2 input image samples.

$$\partial H(\mathbf{V})/\partial[\mathbf{W}] = \partial[\mathbf{W}]/\partial t \tag{4}$$

with respect to the weight matrix $[\mathbf{W}] \equiv (\mathbf{w}_1,\ldots\mathbf{w}_n)$ without the need of a teacher specifying the desired output noise $\mathbf{V} \equiv (v_1,\ldots,v_n)^T$. Algorithmically ANN adjusts the weight matrix *[**W**]* at the linear output range implying the maximum output entropy

$$\mathbf{V}(t) = \tanh([\mathbf{W}]\mathbf{X}(t)) \approx [\mathbf{W}]\mathbf{X}(t) \tag{5}$$

and the "garbage" outputs defined by Gaussian covariance $\langle \mathbf{V}(t)\,\mathbf{V}(t)^T\rangle_G = [I]$. The output means neither YES "1" nor NO "-1" but at the linear MAY-BE range at the "origin 0" where no decision exists implying the maximal output entropy. Consequently, the input information will be kept within as the internal knowledge representation *[**W**]*. The fourth cumulant, the Kurtosis K(**u**), is often used by Helsinki's group to seek the statistical matrix inversion.

$$K(\mathbf{V}) = \langle \mathbf{V}^4\rangle - 3\,(\langle \mathbf{V}^2\rangle)^2 \tag{6}$$

Because of the Gaussian reduction of all higher orders to the second order:

$$\langle \mathbf{v_1v_2v_3v_4}\rangle_G = \langle \mathbf{v_1v_2}\rangle_G \langle \mathbf{v_3v_4}\rangle_G + \langle \mathbf{v_1v_3}\rangle_G \langle \mathbf{v_2v_4}\rangle_G + \langle \mathbf{v_2v_3}\rangle_G \langle \mathbf{v_1v_4}\rangle_G$$

which is further reduced for infinite identical distributive (iid) process to Eq(7). One considers a single weight vector update:

$$d\mathbf{w}/dt = dK/d\mathbf{w} \tag{7}$$

The other weight vectors are found by the projection pursuits. If each voice and image has its unique value of Kurtosis, then seeking a stationary Kurtosis yields the specific voice and image, without knowing what is the desired output.

The lesson we learned from the classical ANN is that one must go beyond the LMS error energy, and apply HOS to ANN. One begins with the Auto-Regression (AR) which extrapolates from the past $\mathbf{X}(t)$ to the future $u_i(t+1) = \mathbf{w}_i^T\mathbf{X}(t)$ by varying the weight vector in minimizing LMS error energy $E = \langle [x(t+1) - u_i(t+1)]^2\rangle$ at the fixed point $\partial E/\partial \mathbf{w}_i = 0$ resulted in an exact Toplitz matrix inversion for a stationary covariance assumption. We generalize AR by a nonlinear output $v_i(t+1) = \tanh(\mathbf{w}_i^T\mathbf{X}(t))$ within $E = \langle [x(t+1) - v_i(t+1)]^2\rangle$, and the gradient descent $\partial E/\partial \mathbf{w}_i = -\partial \mathbf{w}_i/\partial t$. Further generalization is possible because of specific image/speech having a specific histogram whose gray scale statistics departs from that of Gaussian random variable and can be measured by the fourth order cumulant, Kurtosis $K(v_i) = \langle v_i^4\rangle - 3\langle v_i^2\rangle^2$ ($K\geq 0$ super-G for speeches, $K\leq 0$ sub-G for images). ANN has found the internal knowledge representation.

$$[\mathbf{W}] \approx [\mathbf{A}]^{-1}; \qquad [\mathbf{W}]\,\mathbf{X}(t) = [\mathbf{W}][\mathbf{A}]\,\mathbf{S}(t) = [\mathbf{P}][\mathbf{D}]\mathbf{S}(t) \tag{8}$$

which may differ from the unknown IC matrix *[**A**]* within arbitrary permutation order matrix *[**P**]* and the diagonal magnitude *[**D**]*. Taking the advantage of such a natural relaxation of over-sampled millions of sensory neurons, such an information-theoretical and interdisciplinary study has recently reproduced the early vision edge features without a teacher algorithmically. Although it seems to be the inverse requiring only the second order statistics, the search to determine the unknown weight matrix *[W]* do need the high orders of statistics.

2.2 Orthogonal Subspace Projection [Ren & Chang]

The OSP approach has been successfully applied in hyperspectral image processing. In order for the OSP to be effective, the number of bands must be no less than that of signatures to be classified. This ensures that there are sufficient

dimensions to accommodate orthogonal projections resulting from the individual signatures. Such inherent constraint is not an issue for hyperspectral images since they generally have hundreds of bands, which is more than the number of signatures resident within images. However, it is often the case that in multispectral images the number of signatures to be classified is greater than the number of bands, such as 3-band SPOT images and 7-band Landsat TM images. In order for the OSP to be effective, the intrinsic dimensionality (or true dimensionality of data) must be no less than the number of signatures to be classified. This constraint, referred to as Intrinsic Dimensionality Constraint (IDC) requires that the data should have sufficient dimensions to perform orthogonal subspace projection. In this case, each individual signature can be classified in a separate dimension for discrimination. It was found that the OSP performed poorly in discriminating four signatures using 3-band SPOT data, particularly those with similar spectra [26]. More precisely, if we want to classify objects effectively using OSP, each object requires a separate dimension for orthogonal projection. If there is a dimension used to accommodate two or more objects, it is impossible to discriminate these objects using a single dimension through orthogonal projection. However, this problem does not seem to be an issue in hyperspectral data exploitation since hyperspectral images generally have more bands than signatures resident within images, such as 224 bands for AVIRIS data and 210 bands for HYDICE data. As a consequence, the significance of IDC has been overlooked in hyperspectral image processing.

Let $\mathbf{r}_i$ be an $l \times 1$ column vector and denote the *i*-th pixel vector in a multispectral or hyperspectral image where *l* is the number of spectral bands and the bold face is used for vectors. Assume that *M* is an $l \times p$ signature matrix denoted by $(\mathbf{m}_1 \mathbf{m}_2 ... \mathbf{m}_p)$ where $\mathbf{m}_j$ is an $l \times 1$ column vector represented by the *j*-th spectral signature resident in the pixel vector $\mathbf{r}_i$ and *p* is the number of signatures. Let $\boldsymbol{\alpha}_i$ be a $p \times 1$ abundance column vector associated with $\mathbf{r}_i$ given by $(\alpha_{i1}\ \alpha_{i2} \ldots \alpha_{ip})^T$ where α_{ij} denotes the fraction of the *j*-th signature in pixel vector $\mathbf{r}_i$. A linear spectral mixture model for $\mathbf{r}_i$ is described by

$$\mathbf{r}_i = M\boldsymbol{\alpha}_i + \mathbf{n}_i \tag{9}$$

where $\mathbf{n}_i$ is an $l \times 1$ column vector representing additive noise with zero mean and variance $\sigma^2 I$ and *I* is the $l \times l$ identity matrix. We rewrite Eq. (9) as

$$\mathbf{r} = \mathbf{d}\alpha_p + U\gamma + \mathbf{n} \tag{10}$$

where the subscript *i* is suppressed, $U = (\mathbf{m}_1 \mathbf{m}_2 ... \mathbf{m}_{p-1})$ is the undesired spectral signature matrix made up of a set of *p*-1 undesired signatures and $\mathbf{d} = \mathbf{m}_p$ is a desired signature. Here, we assume without loss of generality that the last signature is the desired signature **d**. It should be noted that Eq. (10) can be extended straightforwardly to more than one desired signature. The reason of separating *U* from *M* is to allow us to design an orthogonal subspace projector to annihilate *U* from an observed pixel prior to classification. One such a projector was an undesired signature annihilator given in [20] by

$$P_U^{\perp} = I - UU^{\#} \tag{11}$$

where $U^{\#} = (U^T U)^{-1} U^T$ is the pseudo-inverse of *U* and the notation $^{\perp}_{U}$ in $P_U^{\perp}$ indicates that the projector $P_U^{\perp}$ maps the observed pixel **r** into the range $< U >^{\perp}$, the orthogonal complement of $< U >$. Now, applying $P_U^{\perp}$ to Eq. (10) results in a new spectral signature model

$$P_U^{\perp}\mathbf{r} = P_U^{\perp}\mathbf{d}\alpha_p + P_U^{\perp}\mathbf{n} \tag{12}$$

where the undesired signatures in *U* have been eliminated and the original noise has been suppressed to $P_U^{\perp}\mathbf{n}$. Eq. (12) represents a standard signal detection problem. If the optimal criterion for the signal detection specified by Eq. (12) is chosen to maximize the signal-to-noise ratio (SNR) given by

$$SNR = \frac{(\mathbf{x}^T P_U^{\perp}\mathbf{d})\alpha_p^2 (\mathbf{d}^T P_U^{\perp}\mathbf{x})}{\mathbf{x}^T P_U^{\perp} E[\mathbf{n}\mathbf{n}^T] P_U^{\perp}\mathbf{x}} \quad \text{over } \mathbf{x}. \tag{13}$$

then the maximum SNR of Eq. (13) can be obtained by a matched filter, denoted by M_{d} with $\mathbf{x} = \kappa\mathbf{d}$ where κ is a constant and **d** is the designed matched signal. Based on the approach outlined by Eqs. (12,13), a mixed pixel classification can be carried out by a two-stage process, i.e., an undesired signature annihilator $P_U^{\perp}$ followed by a matched filter, M_{d}. More precisely, if we want to classify a desired signature, say **d** in a mixed pixel based on Eq. (9), we first apply $P_U^{\perp}$ to Eq. (10) to eliminate *U*, then use the matched filter M_{d} to extract **d** from the signal detection Eq. (12). The operator coupling $P_U^{\perp}$ with M_{d} is called an orthogonal subspace classifier, P_{OSP} the one derived in [20] and denoted by

$$P_{OSP} = \mathrm{M}_{\mathrm{d}} P_U^{\perp} = \mathbf{d}^T P_U^{\perp} \tag{14}$$

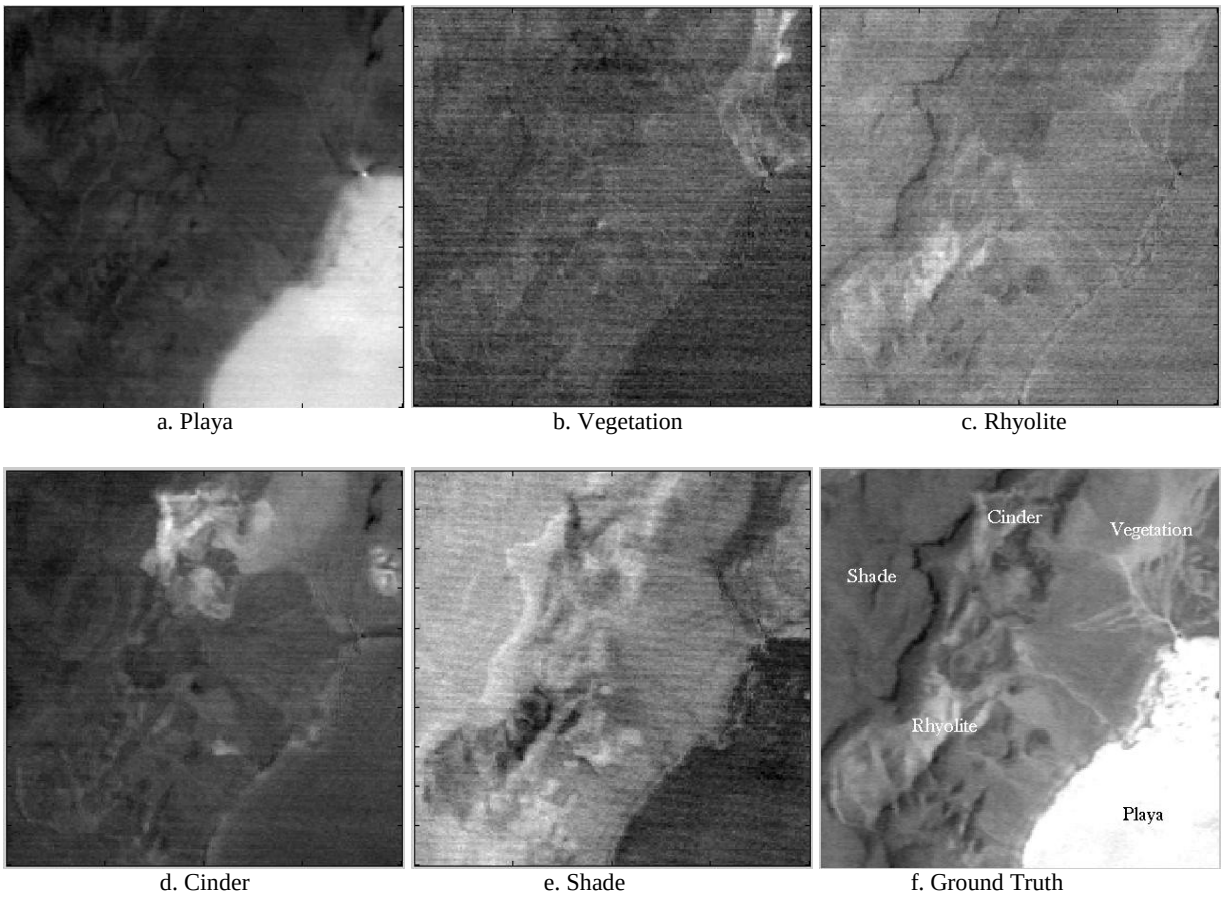

a. Playa b. Vegetation c. Rhyolite

d. Cinder e. Shade f. Ground Truth

Figure 4.a-e. Results produced by the OSP successfully indicated by the bright pixels for five generated object signatures. Figure 4.f Ground truth in these images are read oxidized basaltic cinder, rhyolite, playa (dry lakebed), vegetation and shade.

2.3 AVIRIS Image Results

AVIRIS is an acronym for the Airborne Visible InfraRed Imaging Spectrometer. AVIRIS is a world-class instrument in the realm of Earth Remote Sensing. It is a unique optical sensor that delivers calibrated images of the upwelling spectral radiance in 224 contiguous spectral channels (also called bands) with wavelengths from 400 to 2500 nanometers (*nm*). The instrument flies aboard a NASA ER-2 airplane (a U2 plane modified for increased performance) at approximately 20 *km* above sea level, at about 730 *km/hr*. AVIRIS has flown all across the US, plus Canada and Europe. The science objectives of the AVIRIS project are broad. In a nutshell, the main objective is to identify, measure, and monitor constituents of the Earth's surface and atmosphere based on molecular absorption and particle scattering signatures. Research with

AVIRIS is dominantly directed towards understanding processes related to the global environment and climate change. AVIRIS research areas include: Ecology, Oceanography, Geology, Snow hydrology, Cloud and atmospheric studies.

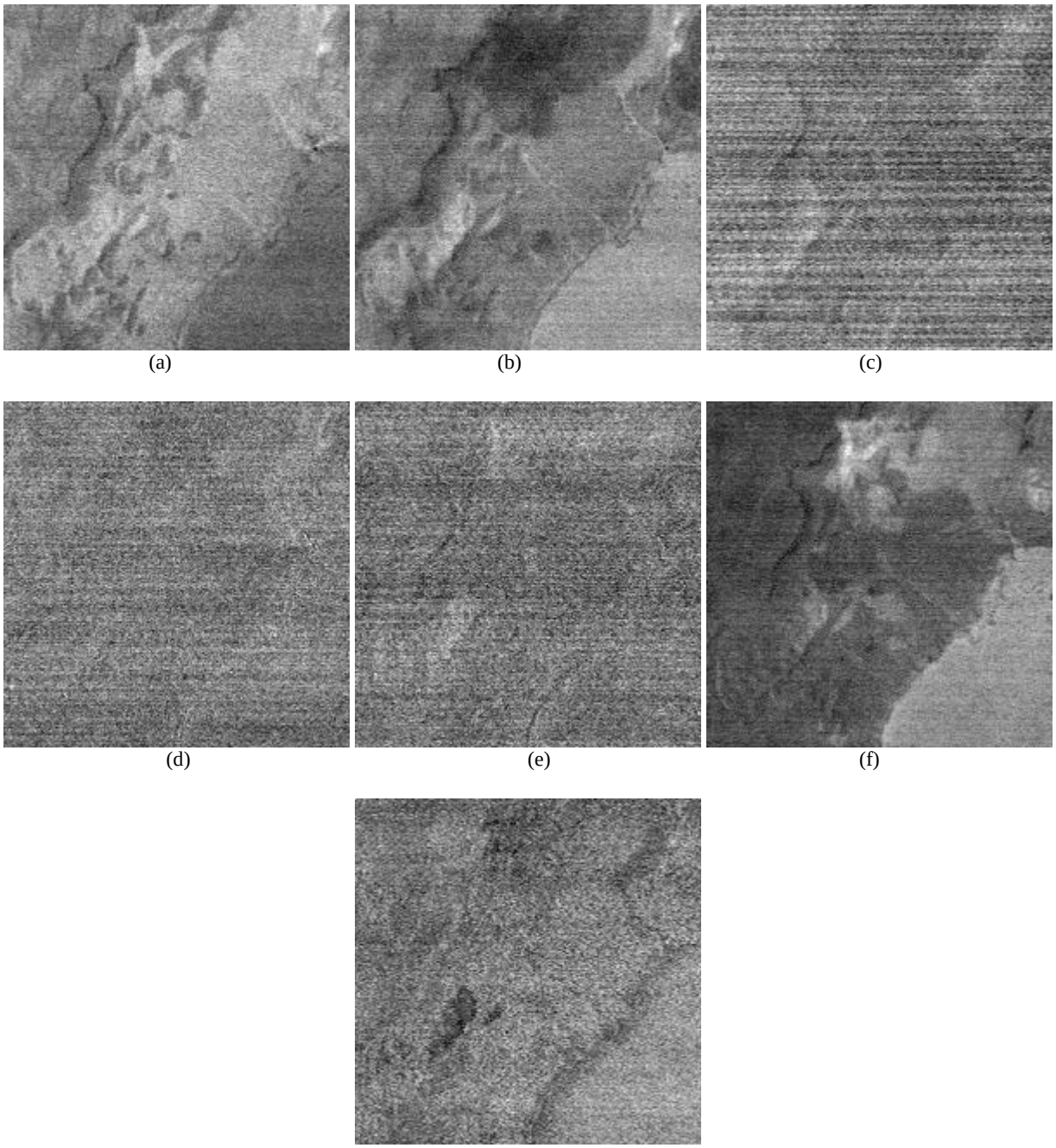

Figure 5. ICA reveals 3 kinds of sensor noise in (c), (d) and (e), creek shown in (b), edge maps, consistent with supervised constrained OSP. (g) reveals the similar Rhyolite information in contrast reverse dark pixels to subplot Figure 4.c.

A set of image data is collected by the AVIRIS system in 158 spectral bands from 0.4 μm to 2.5 μm with *nano* meters spectral resolution and 20 meters GSD. It is a scene of 200x200 pixels extracted the Lunar Crater Volcanic Field in Northern Nye County, Nevada where five signatures of interest in these images are read oxidized basaltic cinder, rhyolite, playa (dry lakebed), vegetation and shade shown in Figure 4.f. Figure 4.a-e show some representative results produced by the OSP using only five generated target signatures. It can be observed that in hyperspectral image classification using more

target signatures usually improves classification performance because there are hundred of bands to accommodate a large number of target signatures that also include natural background signatures, interfering signatures, and clutter. However, since the interfering signature is unknown it is not simple to be classified using supervised OSP. One potential solution to classify the unknown interfering signature is ICA algorithm due to the statistically unsupervised signal classification. Figure 5 shows the simulation results of ICA only using seven bands of signals. It can be noticed that some interfering signatures are classified using ICA unsupervised signal classification. From the experimental results learned, the unsupervised ICA can enhance the performance of the OSP. To apply ICA as an enhancement processor becomes a significant assignment in the follow-up research and development.

3. HIGH DYNAMIC RANGE FOPEN SAR SYSTEM

Synthetic Aperture Radar (SAR) is an airborne or satellite-borne radar system that provides high-resolution maps of remote targets on a terrain or a planet. High dynamic range approach may overcome the long baseline terran curvature (that might otherwise not be suited for the low frequency FOPEN SAR). This theory is also the foundation for many coherent imaging systems in such diverse fields as geophysical exploration and diagnostic medicine. The utility of the wavefront reconstruction theory in SAR was recognized during the inception of these imaging systems in the 1950s and 1960s. However, the lack of fast computing machines and advanced digital signal processing algorithms at that time prevented the development of wavefront reconstruction-based SAR imaging methods. The early SAR systems were based on measurement and optical (analog) processing of the echoed signal using the Fresnel approximation for image formation. This SAR processing in the analog form, or its digital version in late 1970s, is known as range-Doppler imaging. Another SAR imaging method known as polar format processing was introduced for the high-resolution spotlight SAR system in 1970s. This method is based on plane wave approximation.

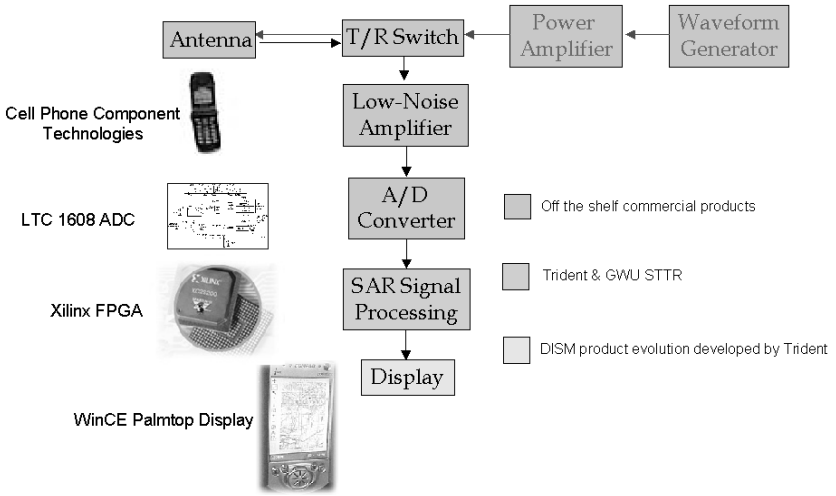

Figure 6. A fully digital inexpensive FOPEN radar system based on COTS components

Foliage Penetration (FOPEN) SAR is a synthetic radar application operated around 500M & 1G Hz that can detect man-made objects concealed by/in dense foliage. Low frequency FOPEN SAR may be used to penetrate foliage and, under certain conditions, even soil. However to differentiate all digital array radar is recommended for high dynamic range A/D (70 dB) without the stage of intermediate frequency. This provides the capability for imaging targets normally hidden by trees, bushes, or other ground cover.

In [25], Trident and GWU plan to build a low cost, low power, high performance, compact, portable, and fully digital Foliage Penetrating Synthetic Aperture Radar (FOPEN SAR) system. In order to make effective use of SAR imagery, an FOPEN SAR system needs to produce high-resolution data at or near real-time. This requires a system that is capable of sustaining the processing rate (nearly 1 Gflop/s) and the data throughput (approximately 10 Mbytes/s). To reduce the cost of such a system, integration of an FPGA-based, digital FOPEN SAR Processor with Commercial-Off-The-Shelf (COTS) components is proposed in [25]. The re-programmability of the Field Programmable Gate Arrays (FPGA's) greatly reduces overall costs, while COTS components can reduce time spent in product development. In the prototype development, the

FOPEN SAR was implemented using VHDL, a hardware description language used in industry to model hardware components, and compared to the FOPEN SAR prototype that was created and verified by using MATLAB. The IEEE 1076.2-1996 Standard VHDL Mathematical Packages were used to provide the necessary mathematical functions. The results showed that the VHDL floating-point FOPEN SAR implementation achieves 290 dB of signal fidelity and processes a 256 x 64 image. This high dynamic range of 290 dB should be able to overcome the long baseline terrain curvature (that might otherwise not be suited for the low frequency such as FOPEN SAR.) The fully digital FOPEN SAR system is shown in Figure 5. For cost efficiency, the FOPEN SAR processor will be integrated with COTS components shown as the blue blocks in Figure 6. The specific required functions, which cannot be implemented using COTS components will be re-designed and implemented in FPGA or DSP. In addition, the control unit, memory, I/O data bus, and other communication interfaces will be designed and integrated within this digital FOPEN radar system.

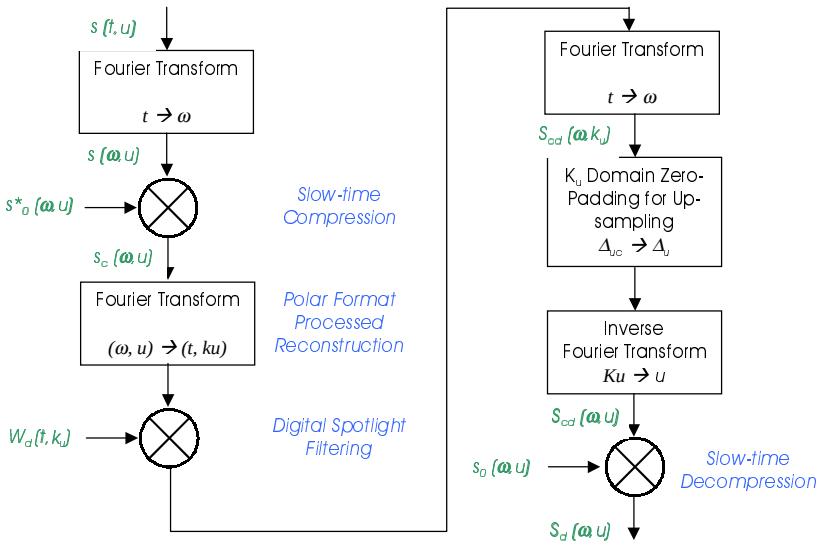

Figure 7. The Block Diagram of A Full Digital Spotlight SAR Algorithm

The purpose of beam steering in the spotlight SAR is to irradiate a finite target area centered around the point (X_c, Y_c) in the spatial domain as the radar is moved along a straight line. The block diagram of full aperture digital spotlight algorithm for spotlight SAR is in Figure 7 and can be summarized as follows. The reference SAR signals is defined via:

$$s_0(\omega,u) = \exp\left[-\, j2k\sqrt{X_c^2 + (Y_c^2 - u)^2}\; + j2kR_c\right] \tag{15}$$

The addition of the phase term $2kR_c$ to the reference signal ensures that the reference fast-time point T_c is unchanged. The digital spotlight filter in the (t, k_u) domain is defined via:

$$W_d(t,k_u) = \begin{cases} 1 & for\ \left|\frac{ct}{2}\cos(\phi+\theta_c) - X_c\right| < X_0 \quad and \quad \left|\frac{ct}{2}\sin(\phi+\theta_c) - Y_c\right| < Y_0 \\ 0 & otherwise \end{cases} \tag{16}$$

Polar format processed resolution with the digital spotlight filter is described as:

$$f_d(t,k_u) = W_d(t,k_u)\,FFT_{(\omega,u)}\left[s_c(\omega,u)\right] \tag{17}$$

Then the digital-spotlighted slow-time compressed SAR signal in the (ω, k_u) domain is obtained via:

$$S_{cd}(\omega,k_u) = FFT_{(t)}\left[f_d(t,k_u)\right] \tag{18}$$

At this point, if the user wishes to up-sample the SAR data within the synthetic aperture u domain (i.e., sample spacing conversion from Δ_{uc} to Δ_u), an appropriate number of zeros should be added to the samples $S_{cd}(\omega, k_u)$ in the slow-time

Doppler k_u domain. After the optional zero-padding in the k_u domain, the digital-spotlight slow-time compressed signal in the (ω, k_u) domain is formed via:

$$s_{cd}(\omega,u) = F^{-1}_{(k_u)}\left[S_{cd}(\omega,k_u)\right] \tag{19}$$

Finally, the digital-spotlighted SAR signal in the (ω, u) domain is constructed from the following slow-time decompression (mixing with the reference SAR signal) shown as follows:

$$s_d(\omega,u) = s_{cd}(\omega,u)s_0(\omega,u) \tag{20}$$

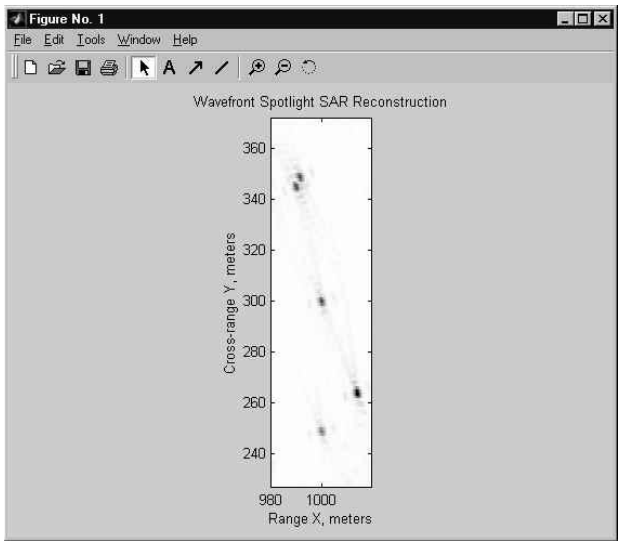

Figure 8. FOPEN SAR using VHDL identical to MATLAB in Figure 9.

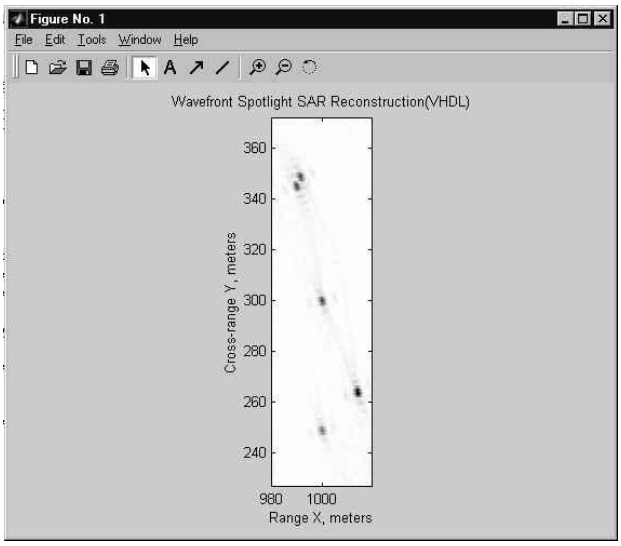

Figure 9. FOPEN SAR using MATLAB

Comparison of the FOPEN SAR results using VHDL implementation to MATLAB implementation was done. Figure 8 shows the FOPEN SAR processing using VHDL, and Figure 9 displays the results using MATLAB. As we can see in Figures 8 and 9, using identical data for the initial input, the VHDL implementation provides a final output that differs from the MATLAB code by 290 dB of signal fidelity, which is directly related to the accuracy imposed upon the VHDL implementation of the algorithm by the use of the IEEE Standard Library. Near real-time processing with 100 dB resolution is feasible by using fixed-point operation in the next development.

In order to improve our FOPEN SAR Processor, we need to complete a number of tasks. From the viewpoint of algorithm development, we need to optimize this FOPEN SAR algorithm in order to reduce the computation complexity. From the VHDL realization, it is also necessary to synthesize the developed FOPEN SAR Processor. Additionally, from the concern of cost and applications, we need to study the trade-off of FPGA versus ASIC implementation. Also, we need to consider a fixed-point processing implementation in terms of speed and accuracy.

4. IFSAR EQUIPPED WITH STOKES POLARIZATION VECTOR

In recent years, IFSAR-derived Detailed Elevation Models have been used in site reconstruction tasks. There are several methods of generating IFSAR data. IFSAR processor with two antennae in a single pass is one of the widely used models. Technically speaking, it is composed of a single aircraft with two antennae, separated by some known displacement named *baseline*, collects all the data from the scene in a single pass. The phase difference between the two returned (one per antenna) generated by a target on the ground is used to determine that target's three-dimensional position.

Stokes Vector is widely used to describe the polarization of the incident and scattered electromagnetic waves in terms of four matrix elements. The modern formulation of polarized light has its origins in the work of G. G. Stokes in 1852.

He introduced four quantities, which are functions only of observable of the electromagnetic wave. These quantities are now known as the Stokes parameters. The elements are: I for total intensity, Q for vertical/horizontal linear polarization, U for 45/135^o linear polarization, and V for left/right circular polarization. These elements give a mathematical representation of what the electromagnetic wave looks like. In order to understand the parameters, image that we have a set of four filters, each of which, under natural illumination, will transmit half of the incident light, discarding the other half. The choice of filters is not a unique one, and a number of equivalent possibilities exist. IFSAR equipped with Stokes polarization vector can precisely provide height information with phase interference discriminate reflection from tree top to bottom end.

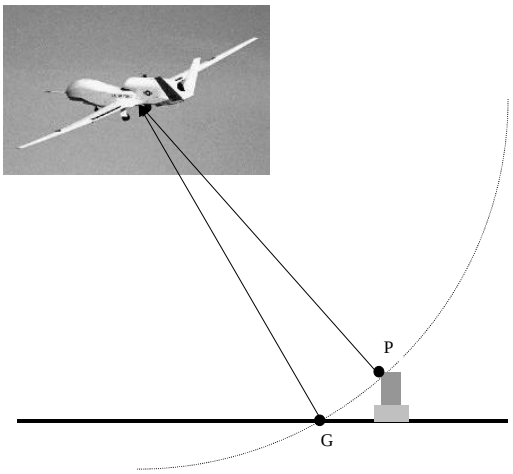

Figure 10: Direct Geometry double ranging method for IF SAR produces Inaccurate Digital Elevation Model (e.g. $Z_P + Z_Q)/2$ reducing the height Zp of the building

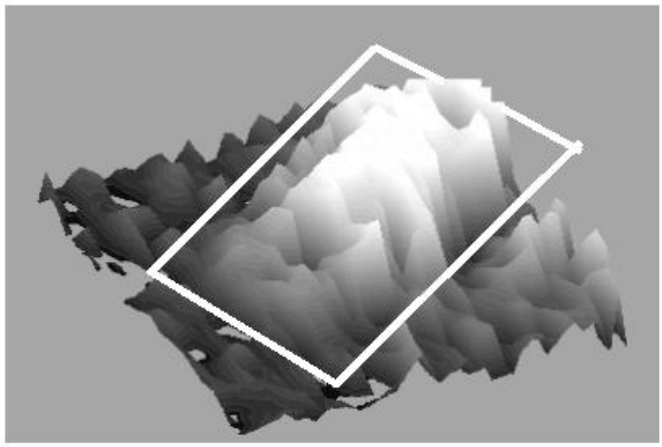

Figure 11: Double Ranging Geometry Method produces Error of building top indicated by a rectangle. Thus, phase interferometer is needed.

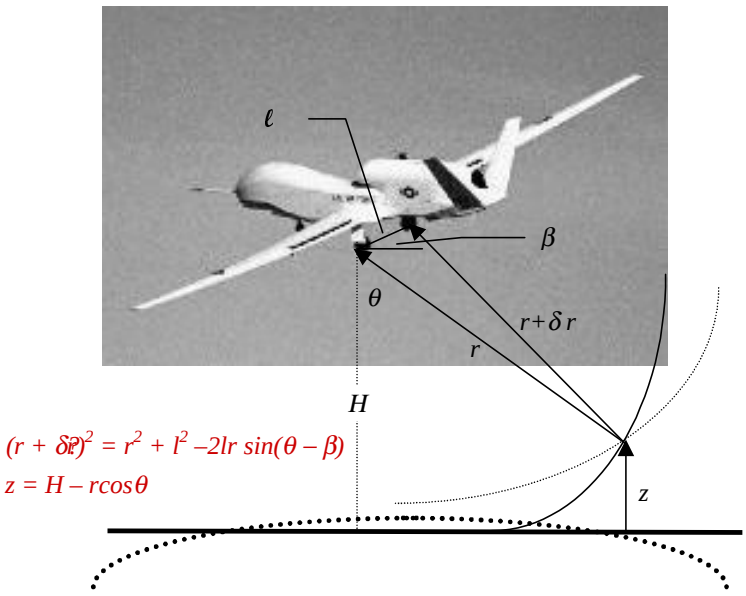

Figure 12. Stereo imaging geometry in the vertical plane of UAV flight direction. The curvature of terrain is indicative, when the time of integration increases due to low frequency IFSAR for FOPEN. Design indicates a high dynamic range may overcome using stereo imaging DAR system in the vertical plane of UAV flight direction. Since the error rate $\frac{\partial Z}{\partial \delta r} = -\frac{r}{l}\frac{\sin\theta}{\cos(\theta-\beta)}$, which is large, we must determine δr *by* interference phase digital measurement with 10-bit accuracy.

IFSAR-derived DEMS are inherently noise and often have a significant amount of data massing from them. As an example of how inaccuracies arise in the elevation data, consider the effects of layover on the front edge of a building. Layover occurs whenever two or more points are at the same distance from the sensor. Figure 10 shows an example of a Global Hawk UAV. In this example, a point P along the front edge of a building has the same range of point G on the ground. Thus, the elevation measured for P will be the average of the heights of point P and G. The phenomenon gives the front edge of a building a crumbled appearance shown in Figure 11. The building's boundary is shown in while lines, and the darker value at the building's front edge indicates that it is at lower elevation than the rest of the rooftop. From Figure 11, it shows that double ranging geometry method produces error of building top indicated by a rectangle. Thus, phase interferometer is needed.

In order to overcome the hurdles, we need to understand IFSAR principles with some preliminary considerations. The paper will be organized as follows. First, we will derive the

elevation using the stereometry method. Discussion is included to end the first section. Then, we will analyze the phase difference of the focused images to provide an interferometric system for the higher elevation accuracy. The next section will outline the IFSAR processing procedure and the intermediate simulation results are included. Finally, we conclude with the related processing: image registration, phase unwrapping, and Geocoding, which lead to the DEM in universal cartographic reference systems.

SAR is widely used to measure (with finite resolution) both azimuth and range of the target. However, it is evident that knowledge of the target range, say r, is insufficient for uniquely determining location of the target and therefore its height above the reference plane (see Figure 10): all the targets within the range beam and located on an equidistance curve are imaged at the same range position. The problem mention in section 1 can be overcome if we consider a second image obtained with a sensor that observes the same scene from different position shown in Figure 12. The spacing between the two sensors is usually referred to as *baseline*; the angle β between the vector connecting the first sensor to the second one and the horizontal direction is referred to as *tilt angle*. The two images can be either obtained by means of a single system with two imaging sensors, or with two repeat passes of a single imaging sensor system. In the latter case, the properties of the scene relevant to the sensing system must remain unchanged with the time frame of the two passes.

A stereometry method to uniquely locate image targets and therefore to determine their heights above the reference plane is easily derived. The target height in Figure 3 is determined by equation (21, 22).

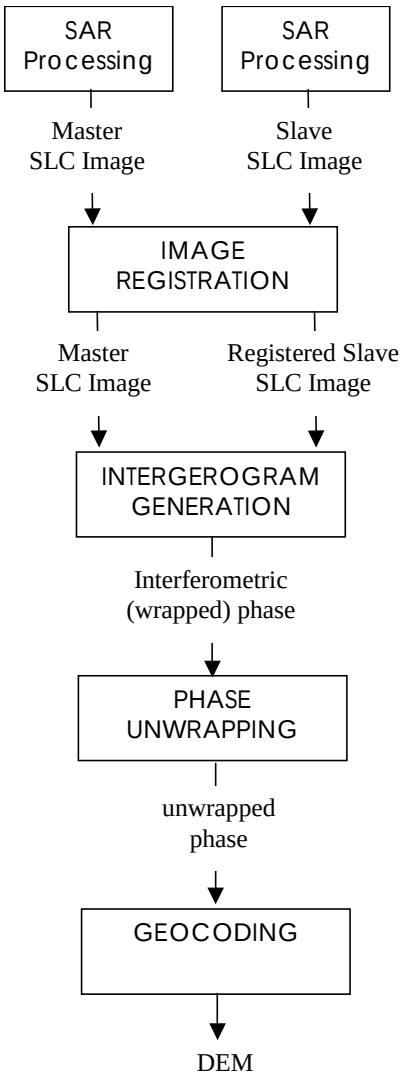

Figure 13. Block diagram of the IFSAR processor for DEM generation

Given r, δr, and both l and b, we can evaluate θ, the target look angle from equation (1). Then the height, z, can be derived using this information in equation (2), where H is the master system height above the reference plane, r is then range of the master image, and $r + \delta r$ is the range of the slave image. The measurement accuracy is limited by the error involved in the evaluation of the path difference δr. This change is determined by searching the same target in the two images, and depends on the range system resolution. It can be observed from the first derivation of equation (21, 22), the height resolution is dependent on the parameter r/l, which is very large in SAR system. For instance, the typical values if ERS-1 SAR system at the scene center: $r = 800m$, $\theta = 23^o$, and the baseline length = $100m$, the height accuracy is about $1.5\ km$. As a conclusion that stereometric techniques are usually inapplicable or characterized by low height accuracy when implemented on SAR systems.

An alternative way to measure δr is carried out by analyzing the phase difference of the focused images. In [27], the accuracy on the path difference, δr, is improved from the meter to centimeter or even millimeter scale. To correctly extract the path difference δr. the images must be properly registered. In other words, they should be correctly superposed to implement the complex conjugate product for each image pixel. The IFSAR processing chain can be summarized as depicted in Figure 13, by the following steps:

(1) Generation of two SLC (Single Look Complex) images via SAR processing if raw data pair relative to the same scene.
(2) Registration of the two SLC images, phase difference extraction.
(3) Phase unwrapping of the wrapping interferometric phase.
(4) Geocoding, the geolocalization of the image points and projection onto universal cartographic grid.

Two SAR receivers image functions and coherent interference are described in Eqs (23-26) and illustrated in Figure 14. Additionally, IF SAR phase function $COS(4\pi/\lambda(R_1(x,y)-R_2\ (x,y)))$ in Figure 15.a v.s. its argument in Figure.15.b for uniform amplitude is demonstrated.

$$(r + \delta r)^2 = r^2 + l^2 - 2lr \sin(\theta - \beta) \tag{21}$$

$$z = H - r\cos\theta \tag{22}$$

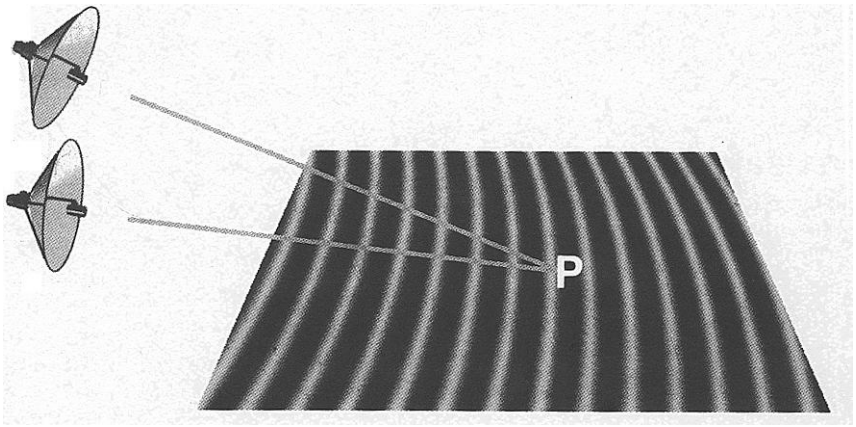

Figure 14. An example of 2 SAR receiver image functions and coherent interference

$$g_1(x,y) \cong a_1(x,y)\exp\left(\frac{j4\pi R_1(x,y)}{\lambda}\right) \tag{23}$$

$$g_2(x,y) \cong a_2(x,y)\exp\left(\frac{j4\pi R_2(x,y)}{\lambda}\right) \tag{24}$$

$$g_1(x,y)g_2^*(x,y) \cong |a(x,y)|^2 \exp\left(\frac{j4\pi}{\lambda}\delta r\right) \tag{25}$$

$$\delta r \equiv (R_1(x,y) - R_2(x,y) \tag{26}$$

We show the standard deviation of the phase digital resolution better then 1^o might overcome the terrain curvature due to low frequency, and long time integration. 1^o is out of 360^o about 10-bit dynamic range.

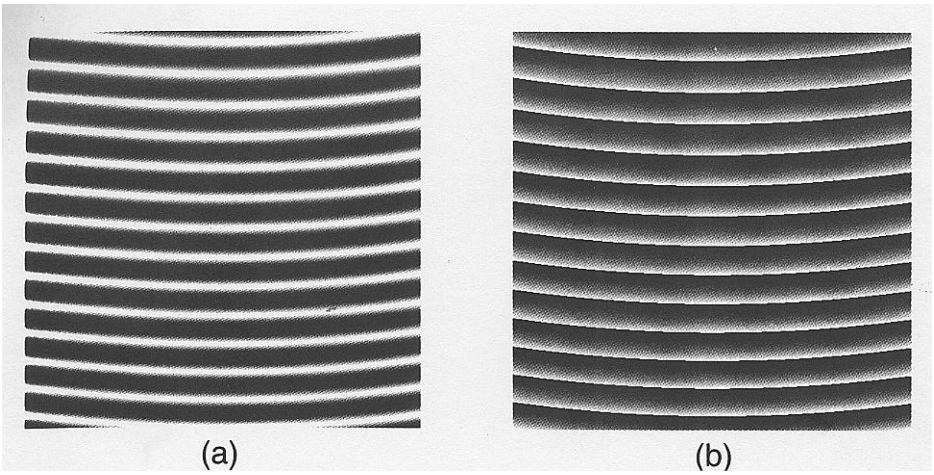

Figure 15 IF SAR phase function COS($4\pi/\lambda(R_1(x,y)-R_2(x,y))$) in Fig.a v.s. its argument in Fig. b for uniform amplitude

5. CONCLUSION

This paper presents a full discussion of Ultraspectral data cylinder of 200 Hyperspectral EO/IR & RF/IF-SAR. We have extended the hyperspectral to include RF spectral for both the foliage penetration (from L band 1 GHz to UHF band 0.5 GHz,) using the polarization RF features and the terrain location ID for navigation registration. We also know that the implementation is feasible to use the matured, COTS components, and the rugged GaAs cellular phone technology due to the lesson learned from the ONR Digital Array Radar (DAR) program for shipboard volume search radar (VSR). Additionally, we have demonstrated the hyperspectral imagery by using the unsupervised learning Independent Component Analyses (ICA) algorithm introduced to the Lansat by Szu [2, 3] since the hyperspectral imagery takes the advantage of more unique spectral signature in terms of the massively parallel artificial neural network computation. We illustrate hyperspectral imagery using the supervised classification orthogonal subspace projections (OSP) with known spectral signatures. Taking the advantage of the high dynamic range ONR DAR VSR technology, we can measure both RF signatures and 3D terrain by means of Interferometric (IF) FOPEN SAR. We prefer a real-time one-path fly over using bi-static Interferometric SAR equipped with a Stokes polarization vector information that can provide us with not only the RF signatures but also terrain height for location ID (knowing terrain contour map stored in the flight data basis). Such an ultraspectral imaging feature-fusion system can manage Forrest search and rescue when it is complement IFSAR FOPEN with EO/IR signatures.

We know that it is very difficult to get useful information from single polarization measurement of UHF SAR. We can obtain lots of bright points from SAR processing but it is hard to know whether they are from tree forks, the ground, or objects under the ground. As an example, our understanding from the counter drug program office is that SOUTHCOM prefers Lynx SAR (Ku Band) for useful foliage penetration because they can tell when they are seeing through a gap in the trees and what they are seeing. In order for UHF to be useful, we need full polarization so we have a clue to identify, which result has been concluded by the NASA Search and Rescue SAR program. Additionally, L band gives very meaningful foliage penetration and is much easier to process, focus, and analyze. The shorter synthetic aperture pays off in a large number of ways. If we want to process IFSAR, differential layover is significantly less. UHF processing can be completed in real time in a quick look mode, but full resolution, phase pure processing and focusing required for interferometry will require a significant time delay. Next, Single Pass UHF IFSAR will be difficult since the ERIM IFSAR uses a *1m* baseline at X-Band, and scaling the baseline with wavelength with a bigger (>25m) baseline for UHF. ERIM failed to put antennas on the wings of a U2 but it might work for P3 or other jumbo airplanes. However, the multi-pass IFSAR has been proved successfully at L and UHF. From our experimental results, we know that polarimetric SAR would be a nice signature complement to hyperspectral, much more so than single polarization. For that matter the C-Band "reflective earth" surface may easily differ from the UHF "bare earth" surface by 30+ meters or more (and assuming everyone is accurate, JPL currently is working to a 16m vertical accuracy target. The way to go for positioning would be the differential GPS/IMU Mike Hess is planning for SHARPs and combine that with what ever level DTED to position the hyperspectral image on the ground. If we don't want to use a super high grade IMU, we can get 1m/km range pointing accuracy with 10cm platform positioning accuracy using Al Evans PTT technology with a cheap IMU. However we need the ultraspectral that have hyperspectral and polarization RF features.

We understand that it is critical to have a high enough power aperture product for UHF. SRI's Impulse UHF radar supposedly can't calibrate on an eight-foot corner reflector. The trade off we have seen between UHF and L band in foliage is that more attenuation at L band than UHF, but that UHF suffers about a 20dB SNR drop relative to L band. The smaller the object, the worse it gets for UHF.

ACKNOWLEDGEMENTS

Authors would like to thank James Buss of ONR, Dr. Hsuan Ren of UMBC, and Dr. George Rogers of NSWCDD for a useful discussion.

REFERENCES

[1] H. Szu, G. Meurer, B. Cantrell, R. Stapleton, “Digital array technology for Radar”, Radar 2000, Wash DC, 2000.
[2] H. Szu, IEEE Circuit & System Newsletter Dec. 99
[3] H. Szu, IEEE Industrial Electronic Newsletter June 99

[4] Telfer B. A., Szu H. H., Chiang R., "Classifying Multispectral data by Neural Networks", Telemetics & Informatics, vol. 10, no. 3, pp. 209-222, 1993
[5] H. Szu and C. Hsu, "Landsat Spectral Demixing à la Superresolution of Blind Matrix Inversion by Constraint MaxEnt Neural Nets," in Wavelet Applications IV, *Proc. SPIE*, **3078**, 1997, 147-160.
[6] H. Szu, C. Hsu, "Blind De-mixing with Unknown Sources", International Conference on Neural Networks, vol. 4, pp 2518-2523, Houston, June, 1997.
[7] Ren, H. and Chang, C.-I, "A generalized orthogonal subspace projection approach to multispectral image classification," *SPIE Conference on Image and Signal Processing for Remote Sensing IV*, Spain, September 1998
[8] Ren, H. and Chang, C.-I, "A computer-aided detection and classification method for concealed targets in hyperspectral imagery," *International Symposium on Geoscience and Remote Sensing'98*, Seattle, WA, July 5-10, pp. 1016-1018, 1998
[9] Adams, J.B., Smith, M.O. and Gillepie, A.R., "Simple models for complex natural surfaces: a strategy for hyperspectral era of remote sensing," *Proc. IEEE Int. Geoscience and Remote Sensing Symposium'89*, pp. 16-21, 1989.
[10] Smith, M.O., Roberts, D.A., Hill, J., Mehi, W., Hosgood, B., Verdebout, J., schmuck, G., Koechler, C. and Adams, J.B., "A new approach to quantifying abundances of materials in multispectral images," *Proc. IEEE Int. Geoscience and Remote Sensing Symposium'94*, Pasadena, CA, pp. 2372-2374, 1994
[11] Sabol, D. E., J. Adams, and M. Smith, "Predicting the spectral detestability of surface materials using spectral mixture analysis." Proceeding of the IEEE International Geoscience Remote Sensing Sump., 2:967-970, 1990F.
[12] Maselli, M. Pieri, and C. Conses, "Automatic identification of end-members for the spectral decomposition of remotely sensed scenes." Remote Sensing for Geography, Geology, Land Planning, and Culturall Hertiage (SPIE) 2960:104-109, 1996
[13] Chang, C.-I and Brumbley, C., "Linear unmixing Kalman filtering approach to signature abundance detection, signature estimation and subpixel classification for remotely sensed images," *IEEE Trans. Aerospace and Electronics Systems*, vol. 37 , pp. 319-330, 1999.
[14] Fukunaga, K., *Introduction to Statistical Pattern Recognition*, 2nd edition, Academic Press, 1990.
[15] Akaike, H., "A new look at statistical model identification," *IEEE Trans. Automatic Control*, vol. 19, pp. 716-723, 1974.
[16] Wax, M. and Kailath, T., "Detection of signals by information theoretic criteria," *IEEE Trans. On Acoustics, Speech and Signal Processing*, vol. 22, pp. 387-392, 1985.
[17] Rissnan, J., "Modeling by shortest data description," *Automatica*, vol. 14, pp. 465-471, 1978.
spectral mixture analysis," *Remote Sensing of Environment*, vol. 59, pp. 472-489, 1997.
[18] Heinz, D.C., Chang, C.-I and Althouse, M.L.G., "Fully constrained least squares-based linear unmixing," *International Geoscience and Remote Sensing Symposium'99*, Hamburg, Germany, 28 June, 1401-1403, 1999.
[19] Tompkins, S., Mustarrd, J.F., Pieters, C.M. and Forsyth, D.W., "Optimization of endmembers for spectral mixture analysis," *Remote Sensing of Environment*, vol. 59, pp. 472-489, 1997.
[20] Harsanyi, J.C. and Chang, C.-I, "Hyperspectral image classification and dimensionality reduction: An orthogonal subspace projection approach," *IEEE Trans. Geosci. Remote Sensing*, vol. 32, pp. 779-785, July 1994.
[21] P. Comon, "Independent Component Analysis: A new concept." Signal Processing 36:287-314, 1994
[22] Bell A. J., Sejnowski T. J., "Learning the high-order structure of a natural sound", vol. 7, *Network: Computation in Neural Systems*, Feb. 1996.
[23] Amari I., Cichocki A., Yang H., "A new learning algorithm for blind signal separation", NIPS 1995, vol. 8, 1996, MIT press, Cambridge, Mass.
[24] Oja E., Karhunen J., "Signal separation by nonlinear Hebbian learning", Proceedings of ICNN-95, pp. 417-421, Perth, Australia, 1995.
[25] S. Arnold, C. Hsu, M. Zaghloul, H. Szu, N. Karangelen, J Buss, "A Fully Digital FOPEN SAR Processor", accepted SPIE (Wavelet Applications VIII), Orlando, April 2001.
[26] Chang, C.-I and Brumbley, C., "Linear unmixing Kalman filtering approach to signature abundance detection, signature estimation and subpixel classification for remotely sensed images," *IEEE Trans. Aerospace and Electronics Systems*, vol. 37 , pp. 319-330, 1999.
[27] L. C. Graham, "Synthetic Interferometer Radar for Topographic Mapping," Proceeding of IEEE, 62, 763

* *szuh@seas.gwu.edu; phone 1-202-994-0880; fax 1-202-994-0223; Digital Media RF Lab., ECE Department, The George Washington University, 725 23rd St., NW, Washington DC 20052*

***hsu@tridsys.com; phone 1-703-267-2313; fax 1-703-2736608; Trident Systems Inc., Fairfax Virginia 22030*